Cellular/Molecular

NMDA Receptor Subunit-Dependent [Ca^{2+}] Signaling in Individual Hippocampal Dendritic Spines

Aleksander Sobczyk,[1,2] **Volker Scheuss,**[1] **and Karel Svoboda**[1]

[1]Howard Hughes Medical Institute, Cold Spring Harbor Laboratory, Cold Spring Harbor, New York 11724, and [2]Department of Physics, State University of New York at Stony Brook, Stony Brook, New York 11794

Ca^{2+} influx through synaptic NMDA receptors (NMDA-Rs) triggers a variety of adaptive cellular processes. To probe NMDA-R-mediated [Ca^{2+}] signaling, we used two-photon glutamate uncaging to stimulate NMDA-Rs on individual dendritic spines of CA1 pyramidal neurons in rat brain slices. We measured NMDA-R currents at the soma and NMDA-R-mediated [Ca^{2+}] transients in stimulated spines ($\Delta[Ca^{2+}]$). Uncaging-evoked NMDA-R current amplitudes were independent of the size of the stimulated spine, implying that smaller spines contain higher densities of functional NMDA-Rs. The ratio of $\Delta[Ca^{2+}]$ over NMDA-R current was highly variable (factor of 10) across spines, especially for small spines. These differences were not explained by heterogeneity in spine sizes or diffusional coupling between spines and their parent dendrites. In addition, we find that small spines have NMDA-R currents that are sensitive to NMDA-R NR2B subunit-specific antagonists. With block of NR2B-containing receptors, the range of $\Delta[Ca^{2+}]$/NMDA-R current ratios and their average value were much reduced. Our data suggest that individual spines can regulate the subunit composition of their NMDA-Rs and the effective fractional Ca^{2+} current through these receptors.

Key words: **NMDA receptor; NR2B subunit; dendritic spines; two-photon; [Ca^{2+}] imaging; glutamate uncaging**

Introduction

Most excitatory synapses terminate on dendritic spines consisting of a spine head connected to the parent dendrite by a thin neck (Harris and Stevens, 1989; Nimchinsky et al., 2002). Dendritic spines compartmentalize chemical signals and thereby facilitate synapse specific signaling (Svoboda et al., 1996; Majewska et al., 2000b; Sabatini et al., 2002; Yasuda et al., 2003). Ca^{2+} can enter the spine through a number of pathways (Sabatini et al., 2001), but of particular importance is Ca^{2+} influx through NMDA receptors (NMDA-Rs) (Muller and Connor, 1991; Yuste and Denk, 1995; Mainen et al., 1999a), which is critical for the induction of long-term changes in synaptic efficacy (Dudek and Bear, 1992; Cummings et al., 1996; Malenka and Nicoll, 1999) and synaptic structural plasticity (Engert and Bonhoeffer, 1999; Maletic-Savatic et al., 1999; Toni et al., 1999). In the hippocampus and neocortex, NMDA-Rs are multimeric channels consisting of the obligatory NR1 subunit and NR2A or NR2B subunits (Kutsuwada et al., 1992; Monyer et al., 1994; Cull-Candy et al., 2001). The expression of different NR2 subunits is developmentally regulated. NR2B-containing receptors dominate in neonatal brain and later are replaced or supplemented with NR2A-containing receptors (Monyer et al., 1994; Sheng et al., 1994; Quinlan et al., 1999). Little is known about the distribution of NR2A- and NR2B-containing receptors at the level of individual synapses.

Most of our knowledge about the biophysical properties of NR2A- and NR2B-containing receptors is based on studies in heterologous systems. NR2A- and NR2B-containing receptors have distinct biophysical properties, including sensitivity to glutamate and deactivation times (Kutsuwada et al., 1992; Monyer et al., 1994; Cull-Candy et al., 2001), and they interact differentially with postsynaptic signal transduction complexes (Bayer et al., 2001). As a result, different receptor subtypes may serve distinct physiological functions in neurons (Vanhoutte and Bading, 2003; Liu et al., 2004; Scimemi et al., 2004). Relatively little is known about the biophysics of NMDA-Rs in the postsynaptic density, where their function is modulated by binding to cytoskeletal and signaling proteins (Sheng and Pak, 2000) and covalent modifications (Yu et al., 1997; Vissel et al., 2001).

Here, we combined (Carter and Sabatini, 2004) two-photon glutamate uncaging (Furuta et al., 1999; Matsuzaki et al., 2001) with two-photon [Ca^{2+}] imaging (Yasuda et al., 2004) to probe the function of synaptic NMDA-Rs. NMDA-R activation produces highly variable [Ca^{2+}] accumulations from spine to spine (Nimchinsky et al., 2004). We find that populations of NMDA-Rs on different spines have different fractional Ca^{2+} currents (the fraction of total current carried by Ca^{2+} ions) and that these differences are dependent on the NMDA-R subunit composition.

Materials and Methods

Preparation and electrophysiology. Acute hippocampal rat brain slices (300 μm thick; postnatal day 16–18) were cut as described previously (Nimchinsky et al., 2004) in accordance with animal care and use guide-

Received March 29, 2005; revised May 12, 2005; accepted May 13, 2005.

This work was supported by NYSTAR, the National Institutes of Health, the Howard Hughes Medical Institute, and the Human Frontiers Science Program (V.S.). We thank Jeff Magee, Bernardo Sabatini, Ryohei Yasuda, and Suzanne Zukin for helpful suggestions and Gordon Shepherd Jr and Karen Zito for comments on this manuscript.

Correspondence should be addressed to Dr. Karel Svoboda, Howard Hughes Medical Institute, Cold Spring Harbor Laboratory, 1 Bungtown Road, Cold Spring Harbor, NY 11724. E-mail: svoboda@cshl.edu.

DOI:10.1523/JNEUROSCI.1221-05.2005

 0270-6474/05/256037-10$15.00/0

lines of Cold Spring Harbor Laboratory. Slices were incubated in gassed (95% O_2/5% CO_2) artificial CSF (ACSF) containing the following (in mM): 127 NaCl, 25 $NaHCO_3$, 25 D-glucose, 2.5 KCl, 1.0 $MgCl_2$, 2.0 $CaCl_2$, and 1.25 NaH_2PO_4 at 34°C for 30–45 min and then at room temperature (22–24°C) until used. Experiments were performed at room temperature in ACSF containing the following (in mM): 0 $MgCl_2$, 3.0 $CaCl_2$, 0.01 2,3-dihydroxy-6-nitro-7-sulfonyl-benzo[*f*]quinoxaline (NBQX), 0.001 TTX, 0.001 thapsigargin, 0.020 ryanodine, 0.010 D-serine, and 2.5 4-methoxy-7-nitroindolinyl (MNI)-caged-L-glutamate. This mixture abolished Ca^{2+} release from intracellular stores, as tested by application of caffeine (Garaschuk et al., 1997) (data not shown). Voltage-clamp whole-cell recordings ($V_{hold} = -70$ mV) from CA1 pyramidal neurons were made with pipettes (4–6 MΩ) containing Cs-based internal solution (in mM): 135 $CsMeSO_3$, 10 HEPES, 10 Na-phosphocreatine, 4 $MgCl_2$, 4 Na_2-ATP, 0.4 Na-GTP, 3 ascorbate, 0.03 Alexa 594 [Ca^{2+}-insensitive red signal (*R*)], and 1 Fluo-5F or 2 Fluo-4FF [Ca^{2+}-sensitive green signal (*G*)]. In approximately one-half of the experiments, we also added 20 mM tetraethylammonium (TEA) to the internal solution and 10 mM TEA to the ACSF. For these experiments, the concentration of $CsMeSO_3$ in the internal solution was reduced to 130 mM. Because TEA did not have an effect, the data were pooled. MNI-caged-L-glutamate, APV, NBQX, and thapsigargin were from Tocris Cookson (Ballwin, MO), TTX was from Calbiochem (La Jolla, CA), Ca^{2+} indicators were from Molecular Probes (Eugene, OR), and all other reagents were from Sigma (St. Louis, MO).

We recorded uncaging-evoked postsynaptic currents (uEPSCs) at the soma (see Figs. 1, 2) (also see supplemental Fig. 2, available at www.jneurosci.org as supplemental material). uEPSC peak size was computed as the mean amplitude of the uEPSC during a 6 ms window around the peak, and the uncaging charge (uQ) was computed as the integrated uEPSCs (Fig. 2*A*). For local drug application (see Fig. 7), we used a picospritzer (Parker Instrumentation, Fairfield, NJ) connected to a glass pipette, located in the vicinity of the imaged dendritic shaft.

Combined two-photon uncaging and [Ca^{2+}] imaging. We used a custom-built combined two-photon uncaging and imaging microscope, powered by two Ti:sapphire pulsed lasers [Mira (Coherent-AMT, Kitchener, Ontario, Canada), tuned to 810 nm for Ca^{2+} imaging; MaiTai (Spectra-Physics, Fremont, CA), tuned to 720 nm for glutamate uncaging]. The intensity of each laser beam was independently controlled with electro-optical modulators (350–80 LA; Conoptics, Danbury, CT). Beams were combined using a dichroic mirror (790SP; Chroma Technology, Brattleboro, VT) and went through the same set of scan mirrors and a 60×, 0.9 numerical aperture objective (Olympus, Melville, NY). Fluorescence was detected by summing epifluorescence and transfluorescence signals, as described previously (Mainen et al., 1999b). The point spread function (PSF) was measured by imaging 0.1 μm beads: the resolution was 0.45 μm laterally and 1.85 μm axially (full width at half maximum of the PSF). Laser power was measured at the back focal plane. The standard uncaging and imaging power was 67 and 10 mW, respectively. Under our conditions, ~25% of this power was transmitted through the objective. Image acquisition and glutamate uncaging were controlled by ScanImage (Pologruto et al., 2003) (http://svobodalab.cshl.edu/software_main.html).

Imaged spines were located on secondary and tertiary apical dendrites within 150 μm from the soma (see Fig. 1*A–C*). To allow for diffusional equilibration of the Ca^{2+} indicator, cells were loaded for at least 20 min before the start of experiments. Imaging trials consisted of eight sequential frames, each 64 ms in duration (see Fig. 1*D*,*E*) (Nimchinsky et al., 2004). We used frame scans, instead of linescans, so that we could monitor spine [Ca^{2+}] and the spread of dendritic [Ca^{2+}] simultaneously. The first frame was acquired with the shutter closed, which allowed the measurement of photomultiplier offsets. The subsequent two frames provided baseline fluorescence. The uncaging stimulus was delivered immediately after the third frame, by turning on the uncaging beam for 0.25 ms while scanning right next to the imaged spine head. Five additional frames were used to monitor [Ca^{2+}] for 320 ms after the stimulus (see Fig. 1*D*,*E*). Each spine was stimulated by glutamate uncaging between five and 12 times at 0.1 Hz. These stimulus trains did not cause any rundown of uEPSC and spine [Ca^{2+}] signals (see supplemental Fig. 8*C*, available at www.jneurosci.org as supplemental material), although longer trains could cause such rundown (data not shown).

The standard uncaging location was ~0.5 μm from the center of the spine head in the direction away from the parent dendrite (see Fig. 1*B*) (also see supplemental Fig. 1*A*, available at www.jneurosci.org as supplemental material). The ratio of spine Δ[Ca^{2+}] over peak uEPSC (denoted as "Δ[Ca^{2+}]/uEPSC" throughout this paper) did not depend on the exact location of the uncaging stimulus (see supplemental Fig. 1*A*, available at www.jneurosci.org as supplemental material). Only spines that were clearly separated from the parent dendrite [range of distances from standard uncaging location to the dendritic shaft surface (*d*), 1–3 μm] (see supplemental Fig. 1*B*, available at www.jneurosci.org as supplemental material) and from other spines (>1 μm away) were stimulated. There was no significant correlation between *d* and uEPSC size (correlation coefficient $r = -0.19$) (see supplemental Fig. 1*B*, available at www.jneurosci.org as supplemental material). Uncaging next to the aspiny regions of the dendritic shaft, at the distances corresponding to typical values of *d*, showed that dendritic currents constituted only ~10% of the total current (see supplemental Fig. 1*C*,*D*, available at www.jneurosci.org as supplemental material). Moreover, NMDA-R currents elicited by uncaging directly on the aspiny dendritic shafts were smaller (approximately three times) than those evoked by uncaging directly next to dendritic spines (supplemental Fig. 1*E*, available at www.jneurosci.org as supplemental material). Together, these data indicate that ~90% of NMDA-Rs stimulated after uncaging were on single dendritic spines.

To measure a fluorescence signal that is proportional to Ca^{2+} through NMDA-Rs, it is important to add sufficient indicator to the cytoplasm to dominate the endogenous buffers of the neuron (Yasuda et al., 2004). This avoids nonlinearities caused by buffer saturation and Ca^{2+}-dependent depression of Ca^{2+} extrusion (V. Scheuss, R. Yasuda, and K. Svoboda, unpublished observations). At the same time, it is important to minimize saturation of the Ca^{2+} indicator even with the large Ca^{2+} accumulations produced by NMDA-R activation. For these reasons, we used high concentrations (1–2 mM) of medium-to-low-affinity Ca^{2+} indicator (K_D, ~1.6 μM for Fluo-5F; K_D, ~10.4 μM for Fluo-4FF) (Yasuda et al., 2004) for our measurements.

The ratio of the change in Ca^{2+}-sensitive green signal over the Ca^{2+}-insensitive red signal was computed in small regions of interest (ROIs) as a measure of the [Ca^{2+}] transient (Yasuda et al., 2003; Nimchinsky et al., 2004) (see Fig. 1). The amplitude of the [Ca^{2+}] transient (Δ[Ca^{2+}]) was calculated as the signal in the first poststimulus frame minus the mean signal of the two baseline frames (see Fig. 1*E*). Under linear conditions, in which Δ[Ca^{2+}] is much smaller than the affinity of the indicator (Yasuda et al., 2004), the concentration of [Ca^{2+}] can be expressed as follows:

$$[Ca^{2+}] = K_D(R/G)_{sat}(G/R), \quad (1)$$

where $(R/G)_{sat}$ is the R/G at saturating [Ca^{2+}], measured in a pipette (Yasuda et al., 2003). Under our standard conditions (1 mM Fluo-5F), we detected even the smallest Δ[Ca^{2+}] with good signal-to-noise ratio using a limited number of trials (see supplemental Fig. 8*A*,*B*, available at www.jneurosci.org as supplemental material). However, under these conditions, there was some dye saturation. Average saturation was ~13%, although some of the larger responses may have been compressed by up to ~50% [estimated by comparing G/R with $(G/R)_{sat}$] (Yasuda et al., 2004). Saturation reduces the larger Δ[Ca^{2+}] and therefore leads to an underestimate of the range of Δ[Ca^{2+}]/uEPSC.

Estimation of spine volume. Spine volumes were measured as described previously (Nimchinsky et al., 2004) by taking the ratio of peak spine brightness (measured as the mean of the pixels at the brightest point of the spine image), which is proportional to the spine volume, over the peak intensity of the big apical dendrite. This value (multiplied by the volume of the PSF in femtoliters) gives the spine volume in femtoliters.

Fluorescence recovery after photobleaching. Fluorescence recovery after photobleaching (FRAP) experiments were performed in line-scan mode with 2 ms time resolution (Svoboda et al., 1996) (see Fig. 5*B*,*C*). We used the uncaging laser to bleach the Ca^{2+}-insensitive dye (Alexa 594) in spines by ~30%, repeated at least five times. FRAP traces were fitted with

single exponentials to determine the recovery time constant τ_{FRAP}, which estimates the strength of spine–dendrite diffusional coupling and is directly related to geometry of the spine neck (Svoboda et al., 1996).

Simulation of [Ca^{2+}] dynamics in single dendritic spines. We modeled free [Ca^{2+}] dynamics in single dendritic spines (Fig. 5*D*) assuming a single compartment model (Neher and Augustine, 1992; Yasuda et al., 2004), as follows:

$$d[Ca^{2+}]/dt = \beta^{-1}(i(t) - e(t)), \quad (2)$$

where $\beta = 1 + \kappa_B + \kappa_{dye}$, with κ_B denoting endogenous and κ_{dye} denoting added buffer capacities (Sabatini et al., 2002). The variables $i(t)$ and $e(t)$ indicate Ca^{2+} influx and efflux to and from the system, respectively. Efflux was modeled as the sum of the linear extrusion of [Ca^{2+}] through pumps and exchangers (Regehr, 1997) and diffusion of [Ca^{2+}] (free and bound to the indicator) via the spine neck, as follows:

$$e(t) = (\Gamma + (1 + \kappa_{dye})\tau_{FRAP}^{-1})([Ca^{2+}] - [Ca^{2+}]_0), \quad (3)$$

where Γ is the extrusion rate constant, τ_{FRAP} is the dye equilibration constant as measured in the FRAP experiments, and $[Ca^{2+}]_0$ is the resting level of [Ca^{2+}]. Equation 2 was solved numerically using a typical uEPSC as influx input, $i(t)$. The following values were used in simulations (Sabatini et al., 2002) (extrusion rate constant was corrected by factor of 3 for room temperature): $\kappa_B = 20$ and $\Gamma = 0.5\ ms^{-1}$.

Coefficient of variation analysis. Which mechanisms dominate the heterogeneity of [Ca^{2+}] signals across spines? To address this question, we performed a coefficient of variation (CV; CV = SD/mean) analysis of $\Delta[Ca^{2+}]$/uEPSC. We assume three independent sources of variation: (1) spine geometry ($CV_{Geometry}$; including variability in spine volume and diffusional coupling between the spine head and parent dendritic shaft), (2) NMDA-R subunit composition ($CV_{Subunit}$), and (3) trial-to-trial fluctuations in the measurements of $\Delta[Ca^{2+}]$/uEPSC for individual spines ($CV_{Fluctuations}$; including dark noise, shot noise, the stochastic nature of glutamate binding to receptors, etc.). CVs of $\Delta[Ca^{2+}]$/uEPSC in the absence ($CV_{Control}$) and presence ($CV_{Ifenprodil}$) of ifenprodil can be expressed as follows:

$$CV^2_{Control} = CV^2_{Geometry} + CV^2_{Subunit} + CV^2_{Fluctuations\ (Control)}, \quad (4)$$

$$CV^2_{Ifenprodil} = CV^2_{Geometry} + CV^2_{Fluctuations\ (Ifenprodil)}. \quad (5)$$

$CV_{Fluctuations} = <CV_{Spine}/\sqrt{n}>$ is the error in estimating the trial-to-trial variability of $\Delta[Ca^{2+}]$/uEPSC based on n trials in one spine, averaged across all spines. The following values were measured: $CV_{Control} = 0.85$ and $CV_{Fluctuations\ (Control)} = 0.20$ (98 spines; 12 cells); $CV_{Ifenprodil} = 0.44$ and $CV_{Fluctuations\ (Ifenprodil)} = 0.21$ (55 spines; six cells). From Equation 5, $CV_{Geometry} = 0.39$. Assuming that $CV_{Geometry}$ is the same for control and ifenprodil conditions, we use Equation 4 to compute $CV_{Subunit} = 0.73$.

Data analysis. On-line and off-line analysis for electrophysiology and Ca^{2+} imaging were performed with custom-written software in Matlab (MathWorks, Natick, MA). Error bars denote SD except for summary data (see Figs. 6, 7), which are given as mean ± SEM. Significance was set at $p = 0.05$ (*t* test). *r* is the correlation coefficient.

Results

Single-spine NMDA-R responses evoked by glutamate uncaging

To probe NMDA-R-mediated Ca^{2+} signals in single spines, we combined two-photon glutamate uncaging with [Ca^{2+}] imaging (see Materials and Methods). Hippocampal CA1 pyramidal neurons were loaded with Ca^{2+}-sensitive (green; 1 mM Fluo-5F) and Ca^{2+}-insensitive (red; 30 μM Alexa 594) fluorophores through whole-cell recording electrodes (Fig. 1*A*). Spines on small secondary and tertiary apical dendrites close to the soma (<150 μm) were imaged in the red channel (Fig. 1*B*). To stimulate synaptic glutamate receptors, MNI-caged-L-glutamate (Matsuzaki et al., 2001) was uncaged with brief (0.25 ms) laser flashes (wavelength, 720 nm) immediately next to the spine head (Fig. 1*B*,*C*). To selectively stimulate receptors on the targeted spine head membrane, we chose spines that were well separated from their parent dendrite and from other spines. Under our experimental conditions, two-photon uncaging released glutamate in a sufficiently small volume so that receptors were excited on individual dendritic spines (supplemental Fig. 1, available at www.jneurosci.org as supplemental material) (see Materials and Methods). The time course of uEPSCs matched the kinetics of spontaneous miniature EPSCs recorded from the same cell, implying that two-photon glutamate uncaging mimics the glutamate transient in the cleft produced by neurotransmitter release (supplemental Fig. 2*A*, available at www.jneurosci.org as supplemental material) (Matsuzaki et al., 2001). uEPSC amplitudes scaled linearly with photolysis time and nonlinearly (exponent, ~2.5) with uncaging power (supplemental Fig. 2*B–D*, available at www.jneurosci.org as supplemental material), as expected for two-photon excitation without depletion of the caged compound or saturation of gluta-

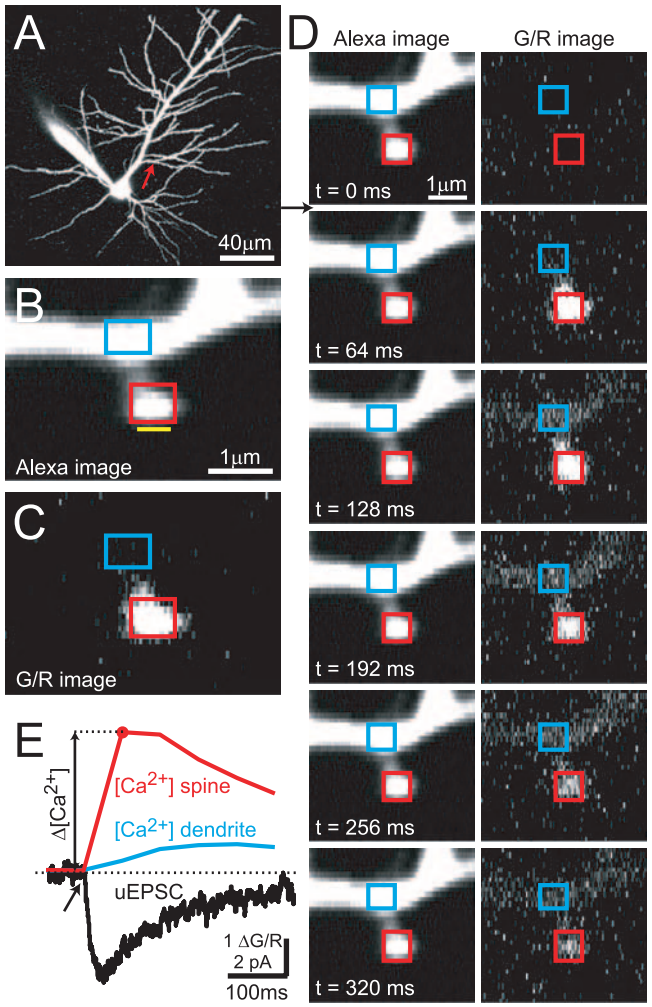

Figure 1. Simultaneous two-photon glutamate uncaging and two-photon [Ca^{2+}] imaging in single dendritic spines. ***A***, CA1 pyramidal neuron filled with Alexa 594. ***B***, Blow-up of a dendritic branch (arrow in ***A***). The yellow bar indicates the position of the uncaging beam. Rectangles denote ROIs for analysis of $\Delta[Ca^{2+}]$ in the spine head (red) and parent dendrite (blue). ***C***, *G/R* image of the [Ca^{2+}] response to glutamate uncaging, averaged over two poststimulus frames (same spine as in ***B***). ***D***, One [Ca^{2+}] imaging trial in frame scan mode (dark frame and the first baseline frame are not shown). The arrow indicates the timing of the uncaging stimulus (same spine as in ***B***, ***C***). ***E***, Uncaging-evoked [Ca^{2+}] transient ($\Delta G/R$) in the spine head (red) and parent dendrite (blue). The simultaneously recorded NMDA-R uEPSC (black) is also shown. The spine is the same as in ***B–D***. Each trace is an average of five trials.

mate receptors. uEPSC could be as big as 30 pA, much larger than average miniature EPSCs (~5 pA), implying that glutamate release from a single vesicle does not saturate synaptic AMPA receptors (AMPA-Rs) (Liu et al., 1999).

To isolate currents and Ca^{2+} influx through NMDA-Rs, experiments were performed in the presence of the AMPA-R blocker NBQX, drugs to reduce dendritic excitation and nonlinearities, and drugs to abolish Ca^{2+} release from intracellular stores (see Materials and Methods). Uncaging reliably induced NMDA-R-mediated uEPSCs and [Ca^{2+}] transients that were primarily restricted to the stimulated spine (Fig. 1*C*,*D*). To avoid membrane depolarization and possible activation of voltage-gated Ca^{2+} channels (VGCCs), the uncaging intensity was limited to keep currents small (mean uEPSC, 4.9 ± 2.6 pA; 98 spines; 12 cells). To further reduce voltage-dependent nonlinearities, Mg^{2+} was omitted from the ACSF.

[Ca^{2+}] transient amplitudes ($\Delta[Ca^{2+}]$) were computed as the change in green fluorescence normalized by red fluorescence (mean $\Delta[Ca^{2+}]$, 1.0 ± 0.7 in dendritic spines). These fluorescence changes correspond to free [Ca^{2+}] changes of 218 ± 154 nM (Eq. 1; see Materials and Methods). Because of the large added Ca^{2+} buffer capacity in our experiments (κ_{dye}, ~625), these Ca^{2+} accumulations were >30 times smaller than they would be in the absence of dye (Sabatini et al., 2002). Both uEPSC and $\Delta[Ca^{2+}]$ were completely blocked by the NMDA-R-specific antagonist APV (100 μM) (supplemental Fig. 3, available at www.jneurosci.org as supplemental material).

Heterogeneity in NMDA-R responses across individual dendritic spines

We next characterized the heterogeneity in NMDA-R responses by measuring uEPSC and $\Delta[Ca^{2+}]$ for multiple spines. To limit differences in dendritic filtering (Hausser et al., 2000) and heterogeneity as a result of synaptic scaling (Magee and Cook, 2000), we stimulated spines that were close to the soma (Fig. 1*A*). For each cell, stimulated spines were on the same dendritic branch within 50 μm from each other. Stimuli were provided with a fixed laser power and caged glutamate concentration over a narrow range of imaging depths in the slice (30–70 μm). uEPSC amplitudes varied from spine to spine (CV = 0.52) (Fig. 2). This variability could be caused by differences in NMDA-R content per spine and/or differences in the amount of free glutamate available to interact with NMDA-Rs. uEPSC amplitudes were proportional to the integrated current (charge) with little scatter, implying that NMDA-R currents evoked on different spines had similar time course (Fig. 2*A*). For each spine, we quantified the spine volume (Nimchinsky et al., 2004). Surprisingly, uEPSC amplitudes did not depend on spine volume (Fig. 2*B*). This suggests that smaller spines have higher densities of NMDA-Rs.

Uncaging-evoked $\Delta[Ca^{2+}]$ also varied from spine to spine (CV = 0.70) (Fig. 3). The CV for $\Delta[Ca^{2+}]$ was larger than for peak uEPSCs. This was expected, because in addition to NMDA-R currents, spine [Ca^{2+}] is shaped by spine geometry, which is highly heterogeneous (Harris and Stevens, 1989). For example, smaller spine heads and longer or narrower spine necks would lead to higher spine Ca^{2+} concentrations.

Next, we compared $\Delta[Ca^{2+}]$ and uEPSC at the level of individual spines. Surprisingly, uEPSC and $\Delta[Ca^{2+}]$ were uncorrelated ($r = -0.05$) (Fig. 3*A*,*B*). Larger NMDA-R currents therefore do not imply larger Ca^{2+} accumulations at the level of individual spines. The ratio $\Delta[Ca^{2+}]$/uEPSC (i.e., the amount of [Ca^{2+}] concentration change per unit of NMDA-R current) varied by a factor of ~10 (because we cannot exclude up to 50% dye saturation for the largest $\Delta[Ca^{2+}]$, the actual range is likely larger; see Materials and Methods) (Fig. 3*C*). There was no obvious morphological feature that could predict spines responding to glutamate uncaging with high or low $\Delta[Ca^{2+}]$ (Fig. 3*A*).

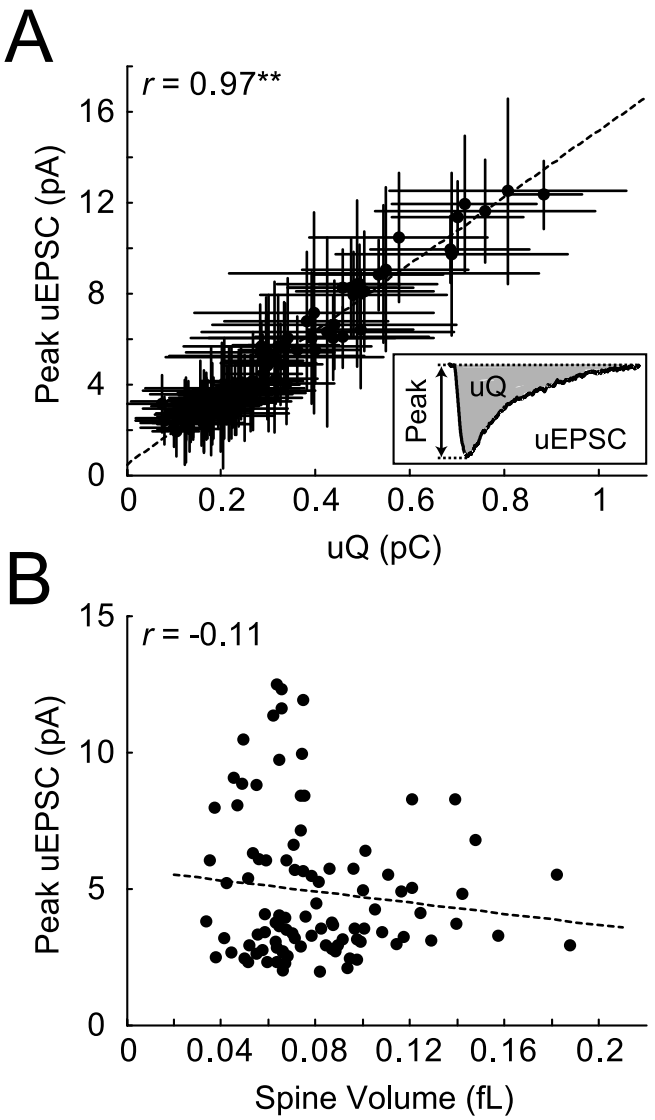

Figure 2. NMDA-R-mediated uEPSCs. ***A***, uEPSC peak amplitude and charge are highly correlated ($r = 0.97$; $^{**}p < 0.001$; 98 spines; 12 cells). Error bars represent SD. ***B***, uEPSC amplitudes are independent of spine volume, implying that smaller spines have higher NMDA-R densities ($r = -0.11$; same dataset as in ***A***).

What mechanisms could contribute to the heterogeneity in NMDA-R-mediated Ca^{2+} signals across spines? Under our experimental conditions, spine [Ca^{2+}] is shaped by geometrical factors such as the spine volume and the spine neck, which determines the diffusional coupling between the spine head and parent dendrite. In addition, regulation of Ca^{2+} influx through NMDA-Rs may play a role. We therefore investigated the role of spine geometry and NMDA-Rs in turn.

Geometric factors underlying the heterogeneity in NMDA-R responses

As expected, spine volume played a role in shaping spine Ca^{2+} signals. $\Delta[Ca^{2+}]$/uEPSC decreased with spine volume, on average (Fig. 4). However, smaller spines displayed the full range of $\Delta[Ca^{2+}]$/uEPSC (e.g., at 0.06 fl in Fig. 4), implying that mecha-

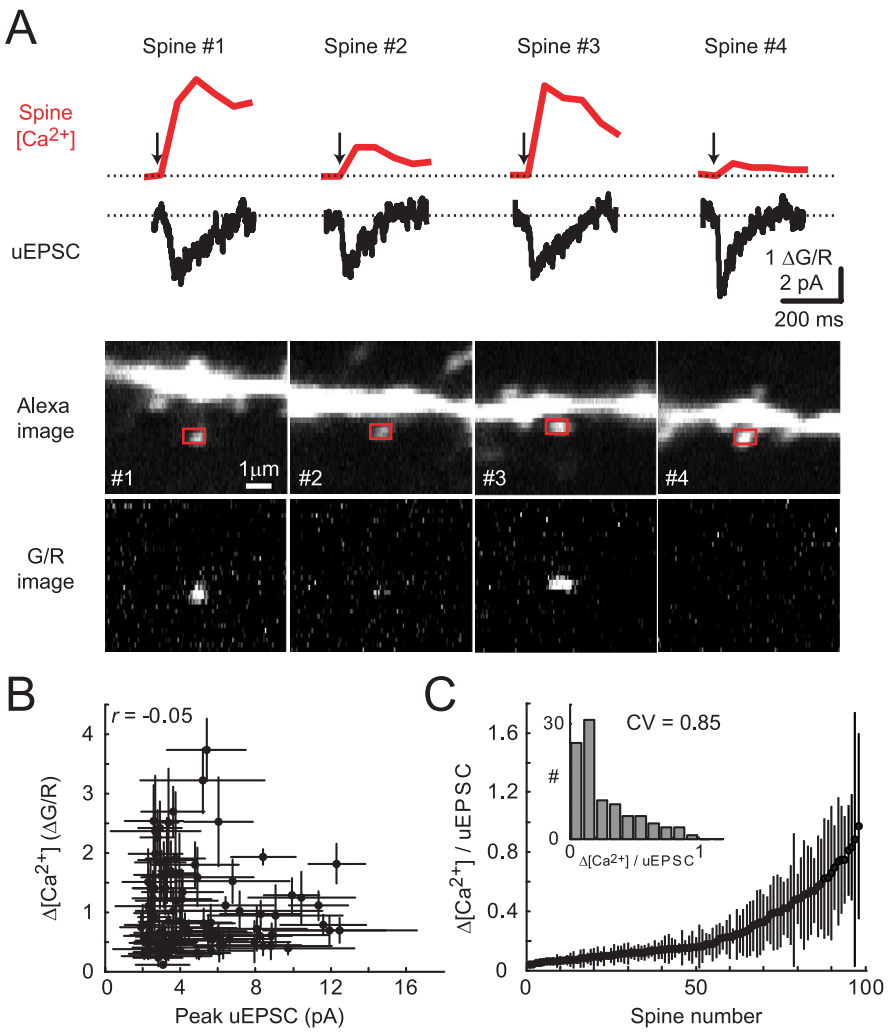

Figure 3. Heterogeneity in [Ca^{2+}] signals across individual dendritic spines. ***A***, Four spines on the same dendritic branch show heterogeneous [Ca^{2+}] transients (top; red) and relatively consistent uEPSCs (middle; black). The corresponding images are also shown (bottom). ***B***, Δ[Ca^{2+}] and uEPSC peak are uncorrelated ($r = -0.05$; 98 spines; 12 cells). ***C***, Rank-ordered distribution of Δ[Ca^{2+}]/uEPSC. Inset, Histogram of Δ[Ca^{2+}]/uEPSC (bin size, 0.1). Error bars represent SD.

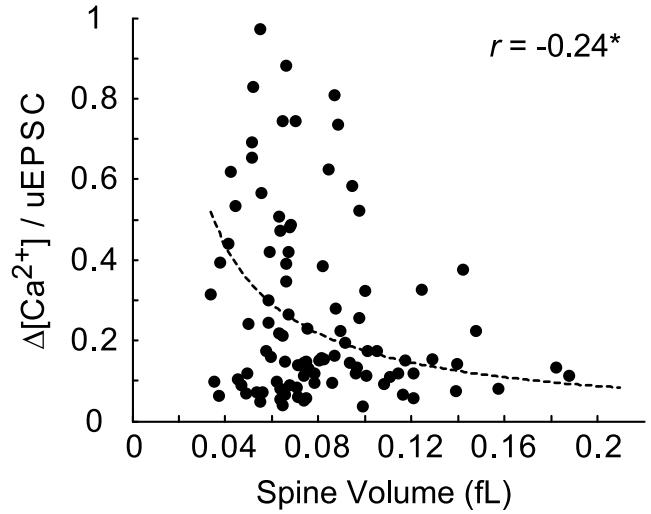

Figure 4. Δ[Ca^{2+}]/uEPSC as a function of spine volume ($r = -0.24$; $^*p < 0.05$; same dataset as in Figs. 2, 3*B*,*C*). The data were fitted to the function constant/(spine volume).

nisms in addition to spine volume contribute to the heterogeneity in [Ca^{2+}] signals.

Next, we tested whether diffusional coupling between spine heads and their parent dendrites could contribute to the observed heterogeneity. Because of the large concentration of Ca^{2+} indicator used in our experiments (1 mM Fluo-5F; corresponding to $\kappa_{dye} \sim 625$), extrusion of Ca^{2+} ions (Regehr, 1997) is slowed by more than a factor of ~30 compared with the unbuffered conditions (Sabatini et al., 2002), and under these conditions, diffusion through the spine neck is likely an important Ca^{2+} clearance pathway from the spine (Majewska et al., 2000a). Spines with stronger diffusional coupling between the spine head and parent dendrite are then expected to have smaller Δ[Ca^{2+}]/uEPSC. Therefore, in the next set of experiments we measured uEPSC, Δ[Ca^{2+}] and spine–dendrite diffusional coupling.

In principle, it is possible to estimate diffusional coupling based on the spread of [Ca^{2+}]-dependent fluorescence signals from the spine to the parent dendrite (Fig. 1*D*). However, this spread is complicated by the dynamics of the NMDA-R current and Ca^{2+} extrusion mechanisms in the spine and dendrite. Instead, we measured diffusional coupling directly using fluorescence recovery after photobleaching (FRAP) of the Ca^{2+}-insensitive red dye (Alexa 594) (parameterized as the recovery time constant τ_{FRAP}) (Fig. 5*B*,*C*). Time constants were in the range 20–200 ms, in agreement with previous measurements (Svoboda et al., 1996; Majewska et al., 2000b).

The example in Figure 5*A*,*B* illustrates that spine geometry cannot account for the heterogeneity in Δ[Ca^{2+}]/uEPSC. Spines 1 and 2 have similar volumes (brightness) and uEPSC amplitudes, but the diffusional coupling is stronger for spine 1 than spine 2. Yet, spine 1 shows several-fold larger Δ[Ca^{2+}] than spine 2. We confirmed this finding for a larger population of spines (41 spines; six cells). As expected, Δ[Ca^{2+}]/uEPSC was positively correlated with τ_{FRAP} ($r = 0.39$; $p < 0.05$) (Fig. 5*C*), implying that bigger Δ[Ca^{2+}] tend to be generated in spines that are diffusionally isolated from their parent dendrites. However, the correlation was weak, and spines with similar diffusional coupling still showed a large range of Δ[Ca^{2+}]/uEPSC. Analysis of spine volume and diffusional coupling taken into account together also failed to account for the heterogeneity in Δ[Ca^{2+}]/uEPSC (supplemental Fig. 4, available at www.jneurosci.org as supplemental material).

In addition, we performed numerical simulations to study the maximal possible effects of diffusional compartmentalization on Δ[Ca^{2+}]/uEPSC. For the same uEPSC, we estimated Δ[Ca^{2+}] for spines with the strongest ($\tau_{FRAP} = 20$ ms) and weakest ($\tau_{FRAP} = 200$ ms) diffusional coupling in our sample. The heterogeneity in diffusional coupling could account for at most a factor of <3 in Δ[Ca^{2+}]/uEPSC (Fig. 5*D*, black traces), whereas experimental data show variability >10 (Figs. 3*C*, 4, 5*C*).

NMDA-R subunit composition

Our analysis shows that spine geometry by itself does not account for the large range in $\Delta[Ca^{2+}]$/uEPSC across individual spines. Instead, we postulate that different spines could contain different types of NMDA-Rs. It could be that individual spines have populations of NMDA-Rs with different deactivation kinetics or fractional Ca^{2+} currents. For example, longer currents would mean larger $\Delta[Ca^{2+}]$ for the same current amplitude. NR2B containing receptors tend to have longer deactivation kinetics than NR2A containing receptors (Cull-Candy et al., 2001) [but these differences can be subtle for endogenous receptors (Barth and Malenka, 2001)].

Are NMDA-R subtypes distributed uniformly across spines? We started by analyzing the uEPSC decay time course. Longer currents were seen in small (<0.07 fl) spines compared with large (>0.11 fl) spines, suggesting that small spines have more NR2B-containing receptors (Fig. 6*A*). Consistent with a role of NMDA-R subunit composition in determining Ca^{2+} signaling, large $\Delta[Ca^{2+}]$/uEPSC were associated with longer currents and vice versa (Fig. 6*A*). Spines with large $\Delta[Ca^{2+}]$/uEPSC thus appear to have more NR2B-containing receptors.

To extend the analysis of NMDA-R subtypes, we applied NR2B-specific NMDA-R antagonists (ifenprodil, Ro 25-6981) (Chizh et al., 2001). We measured NMDA-R mediated responses under baseline conditions (98 spines; 12 cells) and in the presence of ifenprodil (6 μM; 55 spines; six cells) (Fig. 6*A–D*). Experiments were routinely interleaved. All groups of cells had indistinguishable electrophysiological parameters (data not shown) and spine morphologies (i.e., average spine volume; control, 0.08 ± 0.03 fl; ifenprodil, 0.09 ± 0.04 fl). Ifenprodil reduced the average size of uEPSCs by 34.3% (to 3.2 ± 1.1 pA) (Fig. 6*C*, inset), confirming that NR2B containing receptors contribute to the uEPSCs. This block is consistent with the reduction of synaptically evoked NMDA-R currents after application of ifenprodil at CA1 synapses (42% reduction) (supplemental Fig. 5, available at www.jneurosci.org as supplemental material). uEPSC decay time constants were shorter in ifenprodil than under control conditions (Fig. 6*A*), although the difference was modest (~15%). Remarkably, ifenprodil reduced uEPSCs selectively in small spines, implying that large spines may lack NR2B-containing NMDA-Rs (Fig. 6*B*).

We next investigated the role of NMDA-R subunit composition in determining $\Delta[Ca^{2+}]$/uEPSC. Ifenprodil had a large effect on $[Ca^{2+}]$ transients, greatly reducing the heterogeneity in $\Delta[Ca^{2+}]$/uEPSC, especially for small spines (Fig. 6*C*,*D*). Responses with large values for $\Delta[Ca^{2+}]$/uEPSC (>0.4) were absent in ifenprodil (Fig. 6*C*), and the average $\Delta[Ca^{2+}]$/EPSC was reduced (control, 0.27 ± 0.23; ifenprodil, 0.20 ± 0.09; $p < 0.05$). However, the effects of ifenprodil were complex: the incidence of responses with the smallest values $\Delta[Ca^{2+}]$/uEPSC (<0.1) were also reduced (Fig. 6*C*). These experiments suggest that NR2B-containing NMDA-Rs determine the large range of $\Delta[Ca^{2+}]$/uEPSC in small-volume spines.

Ifenprodil causes a reduction in the uEPSC amplitude. It is therefore possible that under control conditions, local voltage escape opens VGCCs and increases $\Delta[Ca^{2+}]$/uEPSC, independent of NMDA-Rs. However, seven experimental observations argue against this possibility. (1) The largest values for $\Delta[Ca^{2+}]$/uEPSC were seen in spines with small uEPSC (Fig. 3*B*). (2) Similar variability in $\Delta[Ca^{2+}]$/uEPSC was observed while holding the recorded neuron at +40 mV, where VGCCs are inactivated (data not shown). (3) Application of (+)-5-methyl-10,11-dihydro-5H-dibenzo [a,d] cyclohepten-5,10-imine maleate (MK-801; 10 μM; six spines; four cells), an NMDA-R subunit-nonspecific antagonist, reduced uEPSCs in a use-dependent manner but did not change $\Delta[Ca^{2+}]$/uEPSC (Fig. 6*E*). (4) uEPSC decreased rapidly with the distance between the uncaging location and the spine head, whereas $\Delta[Ca^{2+}]$/uEPSC was con-

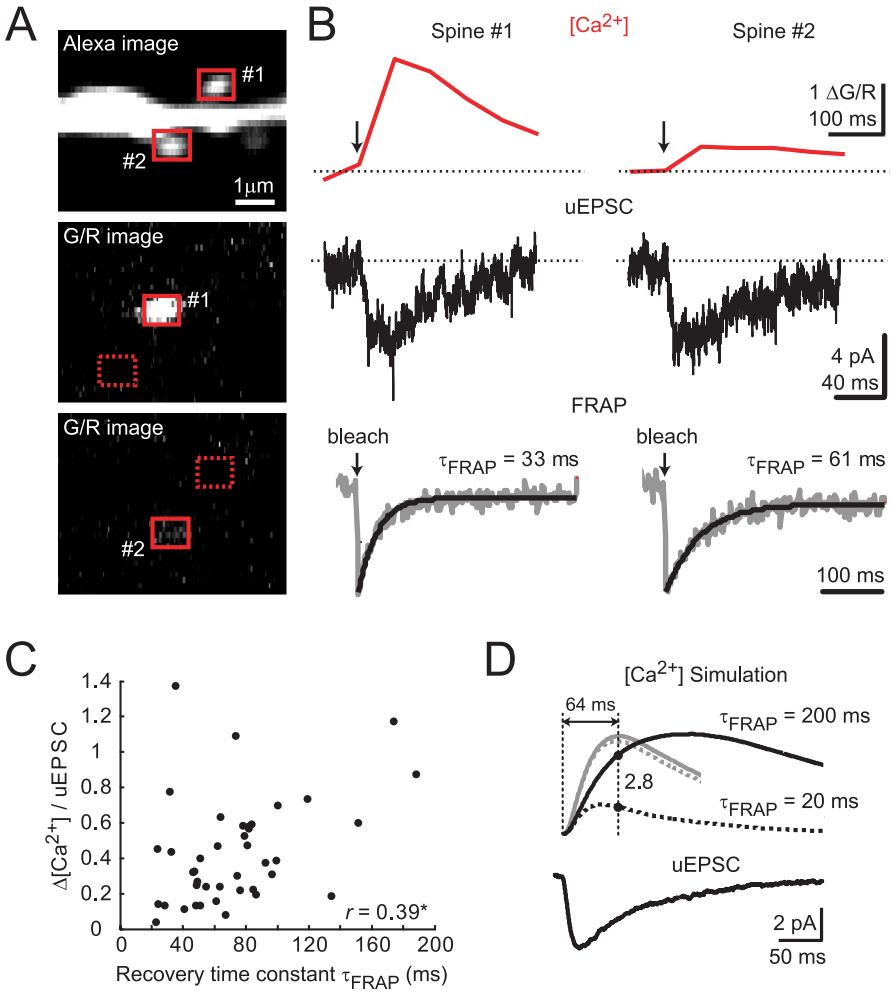

Figure 5. Effects of diffusional coupling across the spine neck on $[Ca^{2+}]$ signals. ***A***, Example of two spines with different $\Delta[Ca^{2+}]$ (1 and 2). An Alexa image of the two spines (top) and *G/R* images after stimulation of spine 1 (middle) or spine 2 (bottom) are shown. ***B***, $\Delta[Ca^{2+}]$ (top) and uEPSC (middle) for spines 1 and 2. FRAP measurements (bottom) for these spines indicate that diffusional coupling is unlikely to explain the observed differences in $\Delta[Ca^{2+}]$. ***C***, $\Delta[Ca^{2+}]$/uEPSC as a function of τ_{FRAP} ($r = 0.39$; *$p < 0.05$; 41 spines; 6 cells). ***D***, Numerical simulations of $[Ca^{2+}]$ dynamics. Top, Simulated $[Ca^{2+}]$ transients (arbitrary units; black traces, 1 mM Fluo-5F; gray traces, no added buffer, scaled down in amplitude by a factor of 15) using the NMDA-R uEPSC (bottom) as an input. $\Delta[Ca^{2+}]$ time courses for extreme values of τ_{FRAP} are shown (200 ms, solid line; 20 ms, dotted line).

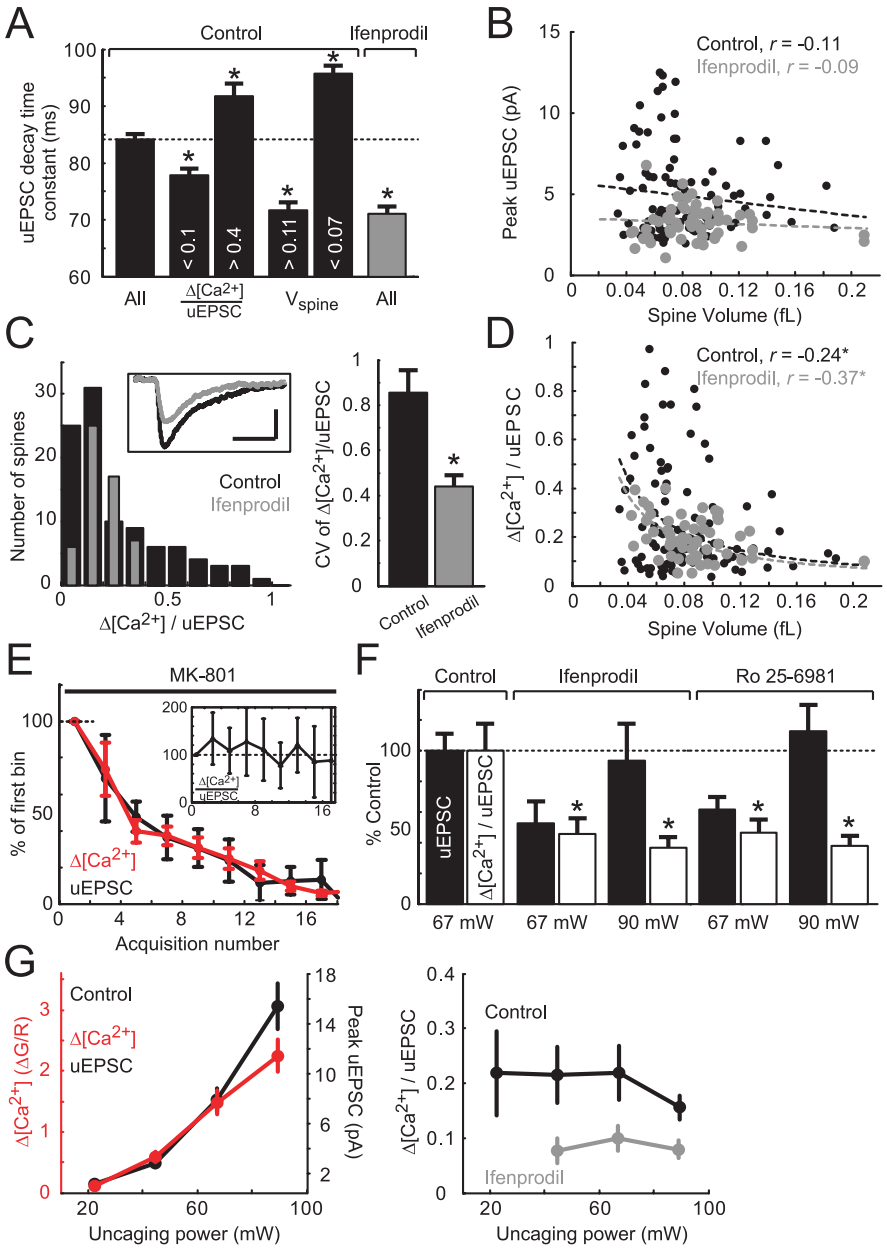

Figure 6. NMDA-R subunit-specific $[Ca^{2+}]$ signals in spines. ***A***, Analysis of uEPSC decay time constants. Far left, All spines in control conditions (black; 84.1 ± 0.9 ms; 98 spines). Middle left, Spines with small (<0.1) and large (>0.4) $\Delta[Ca^{2+}]$/uEPSC ratios (<0.1, 77.8 ± 1.1 ms, 25 spines; >0.4, 91.7 ± 2.3 ms, 23 spines). Middle right, Spines with large (>0.11 fl) and small (<0.07 fl) volumes (>0.11 fl, 71.7 ± 1.3 ms, 14 spines; <0.07 fl, 95.7 ± 1.4 ms, 44 spines). Far right, All spines in 6 μM ifenprodil (gray; 71.0 ± 1.3 ms; 55 spines). ***B***, uEPSC size as a function of spine volume (control, $r = -0.11$; 6 μM ifenprodil, $r = -0.09$). ***C***, Left, Histograms of $\Delta[Ca^{2+}]$/uEPSC in control conditions and in 6 μM ifenprodil. Inset, Average uEPSC in control conditions (black) and in ifenprodil (gray). Calibration: 2 pA, 100 ms. Right, Reduction of CV of $\Delta[Ca^{2+}]$/uEPSC distribution in 6 μM ifenprodil compared with control (control, CV = 0.85; ifenprodil, CV = 0.44). Error bars were computed using the bootstrap method. ***D***, $\Delta[Ca^{2+}]$/uEPSC as a function of spine volume in control conditions (black) and in 6 μM ifenprodil (gray) (control, $r = -0.24$, $^*p < 0.05$; 6 μM ifenprodil, $r = -0.37$, $^*p < 0.05$). For ***A–D***, control, 98 spines, 12 cells (same dataset as in Figs. 2, 3 *B*, *C*, 4); 6 μM ifenprodil, 55 spines, six cells. ***E***, Application of MK-801 (10 μM; 6 spines; 4 cells) blocks $\Delta[Ca^{2+}]$ and uEPSC equally in a use-dependent manner. $\Delta[Ca^{2+}]$ and peak uEPSC were binned (bin size, 2 acquisitions) and normalized to the first bin. Inset, Binned $\Delta[Ca^{2+}]$/uEPSC normalized to the first bin. ***F***, The NR2B subunit-specific antagonists ifenprodil (6 μM; 14 spines; 7 cells) or Ro 25-6981 (0.6 μM; 24 spines; 5 cells) significantly reduced $\Delta[Ca^{2+}]$/uEPSC ($^*p < 0.05$) compared with control (40 spines; 14 cells), independent of uEPSC size (measured at 2 different uncaging laser powers). ***G***, $\Delta[Ca^{2+}]$/uEPSC is independent of uncaging power and uEPSC size. Left, $\Delta[Ca^{2+}]$ and uEPSCs recorded in control condition as a function of uncaging power. Right, $\Delta[Ca^{2+}]$/uEPSC (control, black; 6 μM ifenprodil, gray; same dataset as in ***F***). The divergent point (90 mW) in control conditions is attributable to partial saturation of the Ca^{2+} indicator. Note that in the experiments in ***E–G***, the Ca^{2+} indicator was Fluo-4FF (2 mM). Error bars represent SEM.

stant (supplemental Fig. 1*A*, available at www.jneurosci.org as supplemental material). (5) We further varied the amplitude of the uEPSC in the presence of NR2B-specific antagonists (control, 40 spines, 14 cells; 6 μM ifenprodil, 14 spines, seven cells; 0.6 μM Ro 25-6981, 24 spines, five cells). To minimize saturation of the Ca^{2+} indicator, we used a lower-affinity indicator Fluo-4FF (2 mM) for these experiments. The NR2B-selective blockers reduced $\Delta[Ca^{2+}]$/uEPSC at imaged spines ($p < 0.05$), independent of uEPSC amplitude (Fig. 6*F*). (6) $\Delta[Ca^{2+}]$/uEPSC was independent of uncaging power and thus EPSC size (Fig. 6*G*). (7) Large AMPA-R-mediated uEPSCs failed to open VGCCs to cause $[Ca^{2+}]$ accumulations (supplemental Fig. 6, available at www.jneurosci.org as supplemental material).

Finally, in a smaller number of experiments, we recorded $\Delta[Ca^{2+}]$/uEPSC for the same spines before and after application of ifenprodil (16 spines; four cells) (Fig. 7). In these experiments, ifenprodil was applied locally using a focal puffer glass pipette. Ifenprodil reduced uEPSC by 39.5% (from 4.2 ± 1.4 to 2.5 ± 0.8 pA) (Fig. 7*A*) and caused a significant reduction of $\Delta[Ca^{2+}]$/uEPSC (43.7% reduction; $p < 0.05$) (Fig. 7*B–D*). Spines with higher $\Delta[Ca^{2+}]$/uEPSC were relatively more sensitive to ifenprodil (Fig. 7*B*).

These experiments show that NR2B containing receptors contribute more Ca^{2+} per unit of current, on average. We tested whether this could be explained by the longer deactivation times of NR2B containing receptors by quantifying uEPSCs as integrated charge (Fig. 2*A*). However, $\Delta[Ca^{2+}]$ was still uncorrelated with uQ in control condition ($r = -0.01$) (supplemental Fig. 7*A*, available at www.jneurosci.org as supplemental material). In addition, ifenprodil also reduced variability in $\Delta[Ca^{2+}]$/uQ ($CV_{Control} = 0.83$; $CV_{Ifenprodil} = 0.46$) (supplemental Fig. 7*B*, available at www.jneurosci.org as supplemental material), implying that the longer durations of NR2B mediated uEPSCs do not explain the heterogeneity in $\Delta[Ca^{2+}]$/uEPSC. This is not surprising, because we measured $\Delta[Ca^{2+}]$ early (~64 ms) during each response (Fig. 1*E*), before subunit-dependent differences could have emerged. In addition, the differences in uEPSC time course in spines with high and low $\Delta[Ca^{2+}]$/uEPSC were small (Fig. 6*A*). Instead, we conclude that NR2B-containing receptors in most small spines tend to be associated with large fractional Ca^{2+} currents.

To estimate the relative contributions of spine geometry and NMDA-R subunit

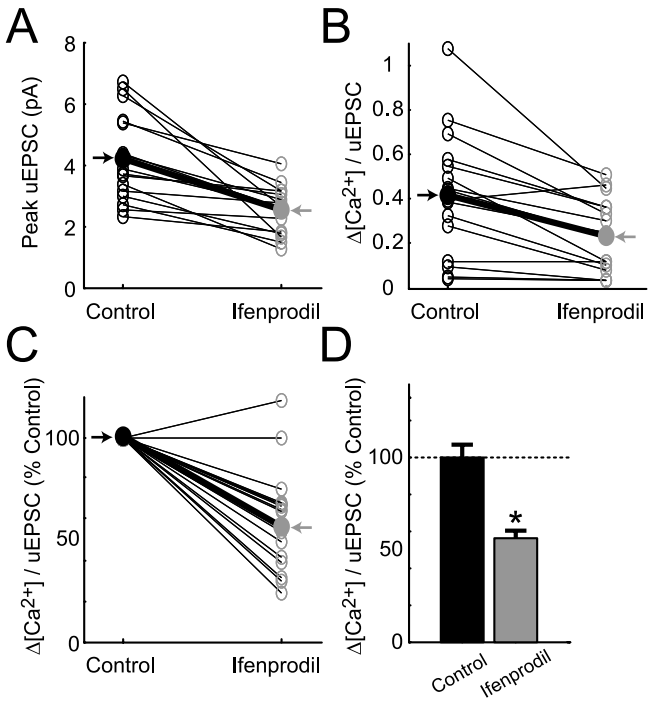

Figure 7. Analysis of NMDA-R-mediated responses before and after local application of ifenprodil. ***A***, Ifenprodil reduces the size of uEPSCs (16 spines; 4 cells; thin lines, individual spines; thick black line, average). ***B***, Ifenprodil reduces $\Delta[Ca^{2+}]$/uEPSC ratios (2 mM Fluo-4FF). ***C***, Same as ***B***, normalized to control. ***D***, Decrease in $\Delta[Ca^{2+}]$/uEPSC after application of ifenprodil (*$p < 0.05$). Error bars represent SEM.

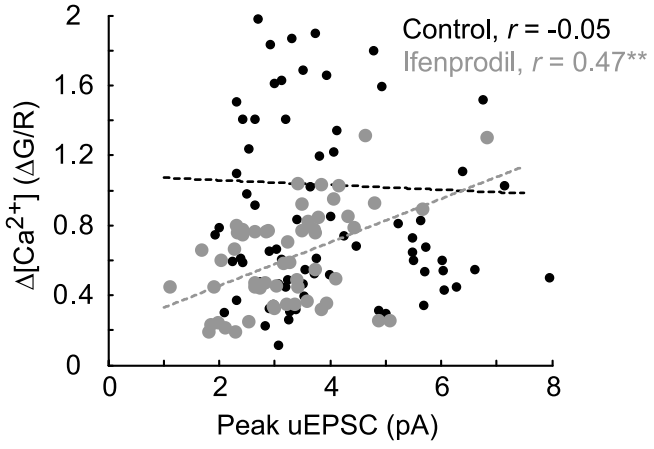

Figure 8. Correlation between $\Delta[Ca^{2+}]$ and uEPSC in the presence of ifenprodil. In control conditions (black), $\Delta[Ca^{2+}]$ and uEPSC are not correlated ($r = -0.05$; 98 spines; 12 cells; data as in Figs. 2, 3 *B*, *C*, 4, 6 *A–D*). In 6 μM ifenprodil (gray; 55 spines; 6 cells; data as in Fig. 6 *A–D*), $\Delta[Ca^{2+}]$ and uEPSC are highly correlated ($r = 0.47$; **$p < 0.001$).

composition in determining the heterogeneity in $\Delta[Ca^{2+}]$/uEPSC, we computed the CV for each component using Equations 4 and 5 (see Materials and Methods). We estimate that more than one-half of the observed heterogeneity in $\Delta[Ca^{2+}]$/uEPSC can be attributed to differential NMDA-R subunit composition across spines. Consistently, in the presence of ifenprodil, $\Delta[Ca^{2+}]$ and uEPSC were strongly correlated ($r = 0.47$; $p < 0.001$) (Fig. 8).

Discussion

Using simultaneous two-photon glutamate uncaging, [Ca^{2+}] imaging, and whole-cell measurement of synaptic currents, we probed NMDA-R-mediated [Ca^{2+}] signaling in single dendritic spines (Fig. 1). These methods allowed us to efficiently probe multiple spines on the same dendritic shaft individually and thus to analyze the heterogeneity in NMDA-R-mediated [Ca^{2+}] signals across individual spines.

The size of glutamatergic currents, both AMPA-R and NMDA-R mediated, increased with uncaging power up to uEPSC amplitudes that greatly exceeded typical miniature EPSCs. These observations provide additional evidence that AMPA-Rs and NMDA-Rs are not saturated by the release of a single synaptic vesicle of glutamate (Liu et al., 1999; Mainen et al., 1999a). We also find that the amplitudes of NMDA-R-mediated uEPSCs is only weakly dependent on spine volume (Fig. 2*B*), confirming that smaller spines have higher densities of functional NMDA-Rs (Takumi et al., 1999; Racca et al., 2000; Nimchinsky et al., 2004). In contrast, the number of AMPA-Rs has been shown to scale with postsynaptic density size (Nusser et al., 1998; Takumi et al., 1999; Matsuzaki et al., 2001). Therefore, small spines are expected to have small ratios of AMPA-R/NMDA-R currents and likely contain so-called "silent" synapses (Isaac et al., 1995; Liao et al., 1995).

The amplitudes of NMDA-R-mediated [Ca^{2+}] transients were highly variable across spines. Surprisingly, $\Delta[Ca^{2+}]$ was not correlated with the amplitude of NMDA-R current; larger NMDA-R currents therefore do not imply larger [Ca^{2+}] accumulations at the level of individual spines (Fig. 3). Consistent with this data, the ratio $\Delta[Ca^{2+}]$/uEPSC varied over more than one order of magnitude. We investigated the mechanisms underlying this heterogeneity. Under our experimental conditions, $\Delta[Ca^{2+}]$/uEPSC depended on geometric factors and NMDA-R subunit composition.

Geometric factors, including spine volume and diffusional coupling between the spine head and parent dendrite, accounted for less than one-half of the observed heterogeneity in $\Delta[Ca^{2+}]$/uEPSC. Because measured fluorescence changes depend on changes in free [Ca^{2+}] concentration, it is not surprising that larger spines tended to show smaller $\Delta[Ca^{2+}]$/uEPSC and vice versa (Nimchinsky et al., 2004). $\Delta[Ca^{2+}]$/uEPSC was also dependent on the diffusional coupling between the spine head and parent dendrite, so that spines with less diffusional coupling tended to have larger $\Delta[Ca^{2+}]$/uEPSC. It should be noted that previous studies have demonstrated that spine–dendrite coupling plays a role in Ca^{2+} clearance from the spine head primarily under conditions when mobile Ca^{2+} buffers (i.e., Ca^{2+} indicator) are added to the cell (Sabatini et al., 2002). For example, under our experimental conditions of high Ca^{2+} buffering and low temperature, extrusion time constants were slowed by more than a factor of 30, while the effective diffusion coefficient of Ca^{2+} is also enhanced (Sabatini et al., 2001). The relationship between $\Delta[Ca^{2+}]$/uEPSC and diffusional coupling we observe is likely not meaningful under physiological conditions.

Remarkably, the subunit composition of NMDA receptors accounted for more than half of heterogeneity in $\Delta[Ca^{2+}]$/uEPSC. Selectively blocking NR2B-containing NMDA-Rs reduced the heterogeneity in $\Delta[Ca^{2+}]$/uEPSC (Fig. 6). However, blocking NR2B-containing receptors did not only eliminate responses with the largest $\Delta[Ca^{2+}]$/uEPSC, but also with the smallest $\Delta[Ca^{2+}]$/uEPSC (Fig. 6*C*). This suggests that individual spines have NR2B containing receptors with different properties, with some spines containing larger fractions of receptors with high (majority of spines) or low (the minority of spines) fractional Ca^{2+} currents. As a result, in the presence of ifenprodil,

$\Delta[Ca^{2+}]$ was highly correlated with the amplitude of the NMDA-R current (Fig. 8).

Fractional Ca^{2+} currents have been measured previously with two distinct approaches. Fluorometric measurements (Schneggenburger et al., 1993; Garaschuk et al., 1996; Schneggenburger, 1996) are considered to be reasonably accurate and have revealed that Ca^{2+} carries ~10% of the NMDA-R current. However, fluorometric approaches have not been used directly to compare NR2A- and NR2B-containing receptors. The second approach depends on shifts in the reversal potential with ionic concentrations. Such measurements have been applied to recombinant NR2A- and NR2B-containing receptors and have not revealed differences in fractional Ca^{2+} current between these receptor subtypes (Monyer et al., 1994). However, the reversal potential method has low sensitivity. In addition, there could be profound differences between recombinant receptors and receptors in synapses. For example, little is known about NMDA-Rs with mixed stoichiometry (e.g., NR1/NR2A/NR2B), which likely form *in vivo*. In addition, recent studies suggest that covalent modifications can alter NMDA-R fractional Ca^{2+} currents (Castillo et al., 2002).

The roles of NMDA-R subtypes in the induction of long-term potentiation (LTP) are controversial. Some studies have argued that NR2B activation promotes long-term depression, whereas NR2A activation promotes LTP (Liu et al., 2004). Other studies in the hippocampus and neocortex have implicated NR2B-containing receptors selectively in the induction of LTP (Tang et al., 1999; Yoshimura et al., 2003). Our data are more consistent with the second view, because NR2B receptors are preferentially expressed in small spines (Fig. 6*A*,*B*,*D*), and LTP is easier to induce in smaller spines (Matsuzaki et al., 2004). It will be interesting to test whether LTP is selectively induced in spines expressing NR2B-containing receptors with large fractional Ca^{2+} currents.

Our findings could have important consequences for *in vivo* plasticity and developmental critical periods. In the barrel cortex, most new spines are transient and small (Holtmaat et al., 2005) and may thus be dominated by NR2B-containing receptors. This is consistent with previous studies on NMDA-R subunits in nascent synapses of cultured neurons (Tovar and Westbrook, 1999). These new spines and their synapses may therefore be particularly plastic, and LTP-like processes could serve to stabilize these spines.

The expression of NR2B-containing receptors correlates with the developmental periods of enhanced plasticity *in vivo* (Kleinschmidt et al., 1987; Fox et al., 1989; Barth and Malenka, 2001). It had been hypothesized that the longer duration of NR2B-containing NMDA-R currents would lead to larger Ca^{2+} accumulations and larger plasticity (Carmignoto and Vicini, 1992; Tang et al., 1999). However, measurements on endogenous receptors have revealed that NR2B content does not necessarily imply long NMDA-R EPSCs (Barth and Malenka, 2001). Our findings suggest that NR2B-containing receptors could provide more Ca^{2+} per unit of current, thereby selectively driving plasticity.

References

Barth AL, Malenka RC (2001) NMDAR EPSC kinetics do not regulate the critical period for LTP at thalamocortical synapses. Nat Neurosci 4:235–236.

Bayer KU, De Koninck P, Leonard AS, Hell JW, Schulman H (2001) Interaction with the NMDA receptor locks CaMKII in an active conformation. Nature 411:801–805.

Carmignoto G, Vicini S (1992) Activity-dependent decrease in NMDA receptor responses during development of the visual cortex. Science 258:1007–1011.

Carter AG, Sabatini BL (2004) State-dependent calcium signaling in dendritic spines of striatal medium spiny neurons. Neuron 44:483–493.

Castillo PE, Chevaleyre V, Goldberg JH, Yuste R, Zukin RS, Bennett MVL (2002) Protein kinase A modulates LTP induction by increasing calcium permeability of NMDA receptors. Soc Neurosci Abstr 28:149.8.

Chizh BA, Headley PM, Tzschentke TM (2001) NMDA receptor antagonists as analgesics: focus on the NR2B subtype. Trends Pharmacol Sci 22:636–642.

Cull-Candy S, Brickley S, Farrant M (2001) NMDA receptor subunits: diversity, development and disease. Curr Opin Neurobiol 11:327–335.

Cummings JA, Mulkey RM, Nicoll RA, Malenka RC (1996) Ca^{2+} signaling requirements for long-term depression in the hippocampus. Neuron 16:825–833.

Dudek SM, Bear MF (1992) Homosynaptic long-term depression in area CA1 of hippocampus and effects of *N*-methyl-D-aspartate receptor blockade. Proc Natl Acad Sci USA 89:4363–4367.

Engert F, Bonhoeffer T (1999) Dendritic spine changes associated with hippocampal long-term synaptic plasticity. Nature 399:66–70.

Fox K, Sato H, Daw N (1989) The location and function of NMDA receptors in cat and kitten visual cortex. J Neurosci 9:2443–2454.

Furuta T, Wang SS, Dantzker JL, Dore TM, Bybee WJ, Callaway EM, Denk W, Tsien RY (1999) Brominated 7-hydroxycoumarin-4-ylmethyls: photolabile protecting groups with biologically useful cross-sections for two photon photolysis. Proc Natl Acad Sci USA 96:1193–1200.

Garaschuk O, Schneggenburger R, Schirra C, Tempia F, Konnerth A (1996) Fractional Ca2+ currents through somatic and dendritic glutamate receptor channels of rat hippocampal CA1 pyramidal neurones. J Physiol (Lond) 491:757–772.

Garaschuk O, Yaari Y, Konnerth A (1997) Release and sequestration of calcium by ryanodine-sensitive stores in rat hippocampal neurones. J Physiol (Lond) 502:13–30.

Harris KM, Stevens JK (1989) Dendritic spines of CA1 pyramidal cells in the rat hippocampus: serial electron microscopy with reference to their biophysical characteristics. J Neurosci 9:2982–2997.

Hausser M, Spruston N, Stuart GJ (2000) Diversity and dynamics of dendritic signaling. Science 290:739–744.

Holtmaat AJ, Trachtenberg JT, Wilbrecht L, Shepherd GM, Zhang X, Knott GW, Svoboda K (2005) Transient and persistent dendritic spines in the neocortex in vivo. Neuron 45:279–291.

Isaac JT, Nicoll RA, Malenka RC (1995) Evidence for silent synapses: implications for the expression of LTP. Neuron 15:427–434.

Kleinschmidt A, Bear MF, Singer W (1987) Blockade of NMDA receptors disrupts experience-dependent plasticity of kitten striate cortex. Science 238:355–358.

Kutsuwada T, Kashiwabuchi N, Mori H, Sakimura K, Kushiya E, Araki K, Meguro H, Masaki H, Kumanishi T, Arakawa M, Mishina M (1992) Molecular diversity of the NMDA receptor channel. Nature 358:36–41.

Liao D, Hessler NA, Malinow R (1995) Activation of postsynaptically silent synapses during pairing-induced LTP in CA1 region of hippocampal slice. Nature 375:400–404.

Liu G, Choi S, Tsien RW (1999) Variability of neurotransmitter concentration and nonsaturation of postsynaptic AMPA receptors at synapses in hippocampal cultures and slices. Neuron 22:395–409.

Liu L, Wong TP, Pozza MF, Lingenhoehl K, Wang Y, Sheng M, Auberson YP, Wang YT (2004) Role of NMDA receptor subtypes in governing the direction of hippocampal synaptic plasticity. Science 304:1021–1024.

Magee JC, Cook EP (2000) Somatic EPSP amplitude is independent of synapse location in hippocampal pyramidal neurons. Nat Neurosci 3:895–903.

Mainen ZF, Malinow R, Svoboda K (1999a) Synaptic calcium transients in single spines indicate that NMDA receptors are not saturated. Nature 399:151–155.

Mainen ZF, Maletic-Savatic M, Shi SH, Hayashi Y, Malinow R, Svoboda K (1999b) Two-photon imaging in living brain slices. Methods 18:231–239.

Majewska A, Brown E, Ross J, Yuste R (2000a) Mechanisms of calcium decay kinetics in hippocampal spines: role of spine calcium pumps and calcium diffusion through the spine neck in biochemical compartmentalization. J Neurosci 20:1722–1734.

Majewska A, Tashiro A, Yuste R (2000b) Regulation of spine calcium dynamics by rapid spine motility. J Neurosci 20:8262–8268.

Malenka RC, Nicoll RA (1999) Long-term potentiation—a decade of progress? Science 285:1870–1874.

Maletic-Savatic M, Malinow R, Svoboda K (1999) Rapid dendritic morphogenesis in CA1 hippocampal dendrites induced by synaptic activity. Science 283:1923–1927.

Matsuzaki M, Ellis-Davies GC, Nemoto T, Miyashita Y, Iino M, Kasai H (2001) Dendritic spine geometry is critical for AMPA receptor expression in hippocampal CA1 pyramidal neurons. Nat Neurosci 4:1086–1092.

Matsuzaki M, Honkura N, Ellis-Davies GC, Kasai H (2004) Structural basis of long-term potentiation in single dendritic spines. Nature 429:761–766.

Monyer H, Burnashev N, Laurie DJ, Sakmann B, Seeburg PH (1994) Developmental and regional expression in the rat brain and functional properties of four NMDA receptors. Neuron 12:529–540.

Muller W, Connor JA (1991) Dendritic spines as individual neuronal compartments for synaptic Ca^{2+} responses. Nature 354:73–76.

Neher E, Augustine GJ (1992) Calcium gradients and buffers in bovine chromaffin cells. J Physiol (Lond) 450:273–301.

Nimchinsky EA, Sabatini BL, Svoboda K (2002) Structure and function of dendritic spines. Annu Rev Physiol 64:313–353.

Nimchinsky EA, Yasuda R, Oertner TG, Svoboda K (2004) The number of glutamate receptors opened by synaptic stimulation in single hippocampal spines. J Neurosci 24:2054–2064.

Nusser Z, Lujan R, Laube G, Roberts JD, Molnar E, Somogyi P (1998) Cell type and pathway dependence of synaptic AMPA receptor number and variability in the hippocampus. Neuron 21:545–559.

Pologruto TA, Sabatini BL, Svoboda K (2003) ScanImage: flexible software for operating laser-scanning microscopes. Biomed Eng Online 2:13.

Quinlan EM, Philpot BD, Huganir RL, Bear MF (1999) Rapid, experience-dependent expression of synaptic NMDA receptors in visual cortex in vivo. Nat Neurosci 2:352–357.

Racca C, Stephenson FA, Streit P, Roberts JD, Somogyi P (2000) NMDA receptor content of synapses in stratum radiatum of the hippocampal CA1 area. J Neurosci 20:2512–2522.

Regehr WG (1997) Interplay between sodium and calcium dynamics in granule cell presynaptic terminals. Biophys J 73:2476–2488.

Sabatini BL, Maravall M, Svoboda K (2001) Ca^{2+} signaling in dendritic spines. Curr Opin Neurobiol 11:349–356.

Sabatini BS, Oertner TG, Svoboda K (2002) The life-cycle of Ca^{2+} ions in spines. Neuron 33:439–452.

Schneggenburger R (1996) Simultaneous measurement of Ca2+ influx and reversal potentials in recombinant *N*-methyl-D-aspartate receptor channels. Biophys J 70:2165–2174.

Schneggenburger R, Zhou Z, Konnerth A, Neher E (1993) Fractional contribution of calcium to the cation current through glutamate receptor channels. Neuron 11:133–143.

Scimemi A, Fine A, Kullmann DM, Rusakov DA (2004) NR2B-containing receptors mediate cross talk among hippocampal synapses. J Neurosci 24:4767–4777.

Sheng M, Pak DT (2000) Ligand-gated ion channel interactions with cytoskeletal and signaling proteins. Annu Rev Physiol 62:755–778.

Sheng M, Cummings J, Roldan LA, Jan YN, Jan LY (1994) Changing subunit composition of heteromeric NMDA receptors during development of rat cortex. Nature 368:144–147.

Svoboda K, Tank DW, Denk W (1996) Direct measurement of coupling between dendritic spines and shafts. Science 272:716–719.

Takumi Y, Ramirez-Leon V, Laake P, Rinvik E, Ottersen OP (1999) Different modes of expression of AMPA and NMDA receptors in hippocampal synapses. Nat Neurosci 2:618–624.

Tang YP, Shimizu E, Dube GR, Rampon C, Kerchner GA, Zhuo M, Liu G, Tsien JZ (1999) Genetic enhancement of learning and memory in mice. Nature 401:63–69.

Toni N, Buchs PA, Nikonenko I, Bron CR, Muller D (1999) LTP promotes formation of multiple spine synapses between a single axon terminal and a dendrite. Nature 402:421–425.

Tovar KR, Westbrook GL (1999) The incorporation of NMDA receptors with a distinct subunit composition at nascent hippocampal synapses *in vitro*. J Neurosci 19:4180–4188.

Vanhoutte P, Bading H (2003) Opposing roles of synaptic and extrasynaptic NMDA receptors in neuronal calcium signalling and BDNF gene regulation. Curr Opin Neurobiol 13:366–371.

Vissel B, Krupp JJ, Heinemann SF, Westbrook GL (2001) A use-dependent tyrosine dephosphorylation of NMDA receptors is independent of ion flux. Nat Neurosci 4:587–596.

Yasuda R, Sabatini BL, Svoboda K (2003) Plasticity of calcium channels in dendritic spines. Nat Neurosci 6:948–955.

Yasuda R, Nimchinsky EA, Scheuss V, Pologruto TA, Oertner TG, Sabatini BL, Svoboda K (2004) Imaging calcium concentration dynamics in small neuronal compartments. Sci STKE 2004:pl5.

Yoshimura Y, Ohmura T, Komatsu Y (2003) Two forms of synaptic plasticity with distinct dependence on age, experience, and NMDA receptor subtype in rat visual cortex. J Neurosci 23:6557–6566.

Yu XM, Askalan R, Keil II GJ, Salter MW (1997) NMDA channel regulation by channel-associated protein tyrosine kinase Src. Science 275:674–678.

Yuste R, Denk W (1995) Dendritic spines as basic functional units of neuronal integration. Nature 375:682–684.